

High-performance solution-processed 2D p-type WSe<sub>2</sub> transistors and circuits through molecular doping

Taoyu Zou<sup>1</sup>, Hyun-Jun Kim<sup>1</sup>, Soonhyo Kim<sup>1,2</sup>, Ao Liu<sup>1</sup>, Min-Yeong Choi<sup>1</sup>, Haksoon Jung<sup>1</sup>, Huihui Zhu<sup>1</sup>, Insang You<sup>1</sup>, Youjin Reo<sup>1</sup>, Woo-Ju Lee<sup>1</sup>, Yong-Sung Kim<sup>2,3\*</sup>, Cheol-Joo Kim<sup>1\*</sup>, Yong-Young Noh<sup>1\*</sup>

<sup>1</sup>Department of Chemical Engineering, Pohang University of Science and Technology, 77 Cheongam-Ro, Nam-Gu, Pohang 37673, Republic of Korea

<sup>2</sup>Korea Research Institute of Standards and Science, Daejeon 34113, Korea

<sup>3</sup>Department of Nano Science, University of Science and Technology, Daejeon 34113, Korea

\*Corresponding authors: Y.-Y. Noh (yynoh@postech.ac.kr), C.-J. Kim (kimcj@postech.ac.kr), and Y.-S. Kim (yongsung.kim@kriss.re.kr)

Keywords: WSe<sub>2</sub> nanosheets; solution process; molecular doping; van der Waals film; thin film transistors; chalcogenide layered p-type semiconductors

## Abstract

Semiconducting ink based on two-dimensional (2D) single-crystal flakes with dangling-bond-free surfaces enables the implementation of high-performance devices on form-free substrates by cost-effective and scalable printing processes. However, the lack of solution-processed p-type 2D semiconducting inks with high mobility is an obstacle to the development of complementary integrated circuits. Here, we report a versatile strategy of

This article has been accepted for publication and undergone full peer review but has not been through the copyediting, typesetting, pagination and proofreading process, which may lead to differences between this version and the [Version of Record](#). Please cite this article as [doi: 10.1002/adma.202208934](#).

This article is protected by copyright. All rights reserved.

doping with Br<sub>2</sub> to enhance the hole mobility by orders of magnitude for p-type transistors with 2D layered materials. Br<sub>2</sub>-doped WSe<sub>2</sub> transistors showed a field-effect hole mobility of more than 27 cm<sup>2</sup> V<sup>-1</sup> s<sup>-1</sup>, and a high on/off current ratio of ~10<sup>7</sup>, and exhibits excellent operational stability during the on-off switching, cycling, and bias stressing testing. Moreover, complementary inverters composed of patterned p-type WSe<sub>2</sub> and n-type MoS<sub>2</sub> layered films are demonstrated with an ultra-high gain of 1280 under a driving voltage ( $V_{DD}$ ) of 7 V. This work unveils the high potential of solution-processed 2D semiconductors with low-temperature processability for flexible devices and monolithic circuitry.

## Introduction

Two-dimensional layered materials (2DLMs) have attracted extensive attention as semiconducting elements for advanced flexible and wearable devices, as well as monolithically integrated devices, because of their excellent electrical and mechanical properties, high crystallinity, and feasible integration to arbitrary systems with dangling bond-free surfaces.<sup>[1]</sup> In particular, single-crystalline flakes of various 2D-materials<sup>[2]</sup> can be dispersed to form semiconducting inks for both n-type and p-type components to realize complementary circuitry by cost-effective graphic art printing techniques with high processability.<sup>[3]</sup> State-of-the-art solution-processed n-type MoS<sub>2</sub> thin-film transistors (TFTs) exhibit a high electron mobility (over 10 cm<sup>2</sup> V<sup>-1</sup> s<sup>-1</sup>) and on/off ratio (approximately 10<sup>6</sup>).<sup>[4]</sup> However, high-performance p-type 2DLMs for solution processes are elusive, hampering the development of complementary logic circuits and high-performance p-n junction devices. P-type 2DLM crystals with intrinsically high mobility, such as black phosphorus, are not applicable to the solution process because of their low chemical stability and low oxidation barrier,<sup>[5]</sup> whereas chemically stable materials, including various transition metal dichalcogenides (TMDs), have shown greatly inferior hole-transport performances, with low mobility (~0.1 cm<sup>2</sup> V<sup>-1</sup> s<sup>-1</sup>) and on/off ratio (~10<sup>2</sup> - 10<sup>5</sup>).<sup>[6]</sup> For multilayer WSe<sub>2</sub> single crystals, selective oxidation of the top surface is known to result in p-type channels.<sup>[7]</sup> However, the

relevant experiments were limited to single-crystal flakes. Uniform oxidation on large-scale, solution-processed films to fabricate arrays of p-type channels with a high carrier mobility is difficult.

Chemically stable p-type 2DLMs have relatively high electron affinities compared to chemically unstable p-type crystals. Therefore, they show a weak tendency to host high hole concentrations, which can be problematic for efficient charge injection and transport. The dispersed flakes in the semiconducting inks possess limited sizes because of the exfoliation process from the bulk crystals and form continuous films by the assembly of individual flakes with numerous inter-flake structures. The electrical resistance of the flake-to-flake interfaces, which reach values as high as 100 G $\Omega$  and more<sup>[8]</sup> can dominate the resistance of a thin film.<sup>[3a, 9]</sup> In addition, high Schottky barriers at the 2D/metal electrode interface by Fermi level pinning can result in high contact resistance at channels with low carrier concentrations.<sup>[10]</sup>

Doping in 2DLMs, such as atomic substitution,<sup>[11]</sup> molecular,<sup>[12]</sup> and electrostatic doping,<sup>[13]</sup> is the most fundamental strategy for controlling carrier concentration and device performance. However, it is difficult to implement atomic substitution in liquid-phase exfoliated nanoflakes, and sophisticated device structures with separate-gate configurations are required for electrostatic doping. Molecular p-type doping is an easy and widely used method for controlling the hole carrier density because it accepts electrons from the host 2D semiconductor or by dipolar interactions. However, most doping molecules can only lay on the TMD surface; they cannot easily penetrate the interspace or interface because of their large size,<sup>[14]</sup> which may cause non-uniform doping in 2D thin films with stacked nanoflakes. Gas molecules and acids with small molecules act as defect-oriented dopants by bonding at the defect sites<sup>[15]</sup> or by forming oxide layers.<sup>[7a, 16]</sup> Therefore, it is challenging to achieve stable and effectively controllable molecular p-doping in solution-processed thin films composed of stacked nanoflakes.

In this work, we report a simple but effective way to improve the performance of solution-processed p-type TMD TFTs by doping with Br<sub>2</sub> molecules. The Br<sub>2</sub>-doped WSe<sub>2</sub> TFTs showed a field-effect mobility ( $\mu_{FE}$ ) of 27 cm<sup>2</sup> V<sup>-1</sup> s<sup>-1</sup>, which is orders of magnitude larger than 4 × 10<sup>-3</sup> cm<sup>2</sup> V<sup>-1</sup> s<sup>-1</sup> achieved with undoped devices, along with a near-zero threshold voltage ( $V_{TH}$ ) and an on/off current ratio of over 10<sup>7</sup>. Density functional theory (DFT) calculations showed that the Br<sub>2</sub> molecules could physically adsorb on WSe<sub>2</sub> surfaces up to a coverage of >1/4, and create shallow acceptor states near the valence band maximum ( $E_{VBM}$ ). Br<sub>2</sub> molecules can effectively dope nanoflakes, contacts, interflake boundaries, and flake-gate dielectric interfaces owing to their small size. Four-point probe measurements and temperature-dependent measurements showed improved  $\mu_{FE}$  values, which were attributed to the reduced contact resistance through a low Schottky barrier height and efficient channel charge transport. Moreover, the Br<sub>2</sub>-doped WSe<sub>2</sub> TFTs exhibited outstanding on-off switching, cycling, and bias-stressing stability. Finally, solution-processed high-performance CMOS inverters composed of integrated p-WSe<sub>2</sub> and n-MoS<sub>2</sub> TFTs were demonstrated with a high gain of over 1200.

## 2. Results and Discussions

Various semiconducting inks with different p-type TMD nanosheets (**Figure 1a**) were first prepared via electrochemical exfoliation with a large ammonium cation molecule (tetraheptylammonium bromide),<sup>[4]</sup> followed by rinsing and centrifugation (see Methods). We chose the molecular intercalant to minimize defect formation from the intercalation process, resulting in semiconductor nanosheets with large lateral sizes,<sup>[2d]</sup> and use the liquid cascade centrifugation (LCC) method to realize a narrow thickness distribution of nanoflakes.<sup>[17]</sup> The average lateral size and thickness of the exfoliated WSe<sub>2</sub> nanosheets were measured to be approximately 800 nm and 2.5 nm (equivalent to 3-4 layers), respectively, by atomic force microscopy (AFM) (Figure 1b and Figure S1). High-resolution transmission electron microscopy (HRTEM, Figure 1c) and large-view atomic-resolution scanning transmission

electron microscopy (STEM, Figure S2) revealed high crystallinity and high-quality surfaces on the exfoliated flakes, without noticeable defects such as vacancies. Furthermore, the UV–visible absorption spectrum and Raman spectrum of the exfoliated TMDs showed only the characteristic peaks of the crystals without signals from absorbed contaminants (Figure S3 and S4).

The optimized drop-casting of TDM inks resulted in continuous films constructed of stacks of lateral arrays of TMD flakes with high density and effective inter-flake overlaps (Figure 1d). Scanning electron microscopy (SEM) showed a compact thin film with a distinguishable intensity from the bare substrate region (Figure 1e). Cross-sectional TEM (Figure 1f) revealed a film with a nominal thickness of  $\sim 10$  nm, where multiple flakes overlapped with clean interfaces, and the layered structures were parallel to the surface. The aligned stacking orientation was further confirmed over a macroscopic scale by X-ray diffraction (XRD) with a characterization area of  $\sim 1$  cm<sup>2</sup>. The observed out-of-plane diffraction peaks were consistent with the interlayer distance of 0.65 nm for pristine WSe<sub>2</sub> crystals (Figure S5).<sup>[1d]</sup>

TMD films were patterned using a lift-off-based photolithography method to fabricate an array of channels for TFTs (see Methods for details) (Figure S6). We first patterned the photoresist (PR) via a photolithography process to define the deposition area for the semiconductor inks. Then, the photoresist was peeled off to form a batch-fabricated array of 2D TMDs with the desired patterns on a 4-inch wafer of a Si/SiO<sub>2</sub> substrate (Figure 1d) or another substrate such as a glass or flexible PEN substrate (Figure S7). Our method has the advantages of fabricating large-area flexible or even wearable circuits with a low cost and easy process using 2D functional inks.

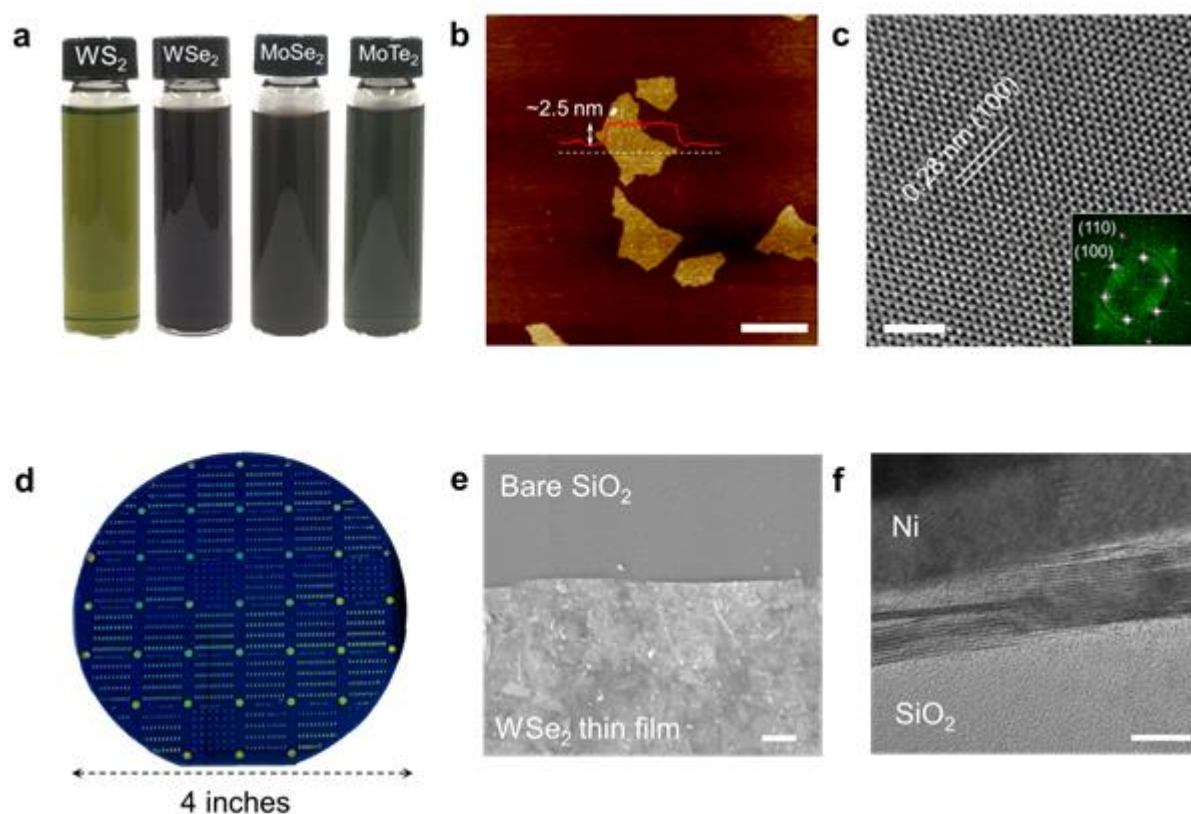


**Figure 1. 2D TMDs solution and large-area patterned film.** **a**, Photograph of exfoliated TMD nanosheets dispersed in isopropanol. **b**, AFM image of exfoliated WSe<sub>2</sub> nanosheets. WSe<sub>2</sub> flakes with a lateral dimension of 0.5–1 μm and thickness of ~2.5 nm (scale bar, 800 nm). **c**, High-resolution TEM image of exfoliated WSe<sub>2</sub> nanoflake. Inset is the selected-area electron diffraction image. The interlayer distance of the (100) planes is 0.28 nm from the electron hexagonal diffraction pattern (scale bar, 2 nm). **d**, Photograph of patterned 2D TMD thin film on a standard 4 inch Si/SiO<sub>2</sub> wafer. **e**, SEM image of the patterned WSe<sub>2</sub> thin film (scale bar, 1 μm). **f**, Cross-sectional TEM image of the WSe<sub>2</sub> thin film on the Si/SiO<sub>2</sub> substrate (scale bar, 10 nm).

The electrical properties of the solution-processed WSe<sub>2</sub> TFT arrays were investigated (**Figure 2a**, **Figure S8a**). The optimized thickness of the WSe<sub>2</sub> film for the channel was approximately 40 nm, as measured by AFM (**Figure S8b**). The  $I_{DS}-V_{GS}$  transfer curve of

pristine WSe<sub>2</sub> transistors exhibited typical n-type dominant ambipolar characteristics, with a very low  $\mu_{FE}$  of  $4 \times 10^{-3} \text{ cm}^2 \text{ V}^{-1} \text{ s}^{-1}$  (Figure 2b), which was measured from the transconductance curve using a capacitance model (Figure S9). The low on-state current ( $I_{on} \sim 10^{-9} \text{ A}$  at  $V_{GS} = -5$ ) and a large negative threshold voltage ( $V_{TH}$ ) of  $-3.5 \text{ V}$  indicated the small conductance and low intrinsic hole carrier concentration. Based on the high crystallinity of WSe<sub>2</sub>, as confirmed above, the channel conductance and transistor performance could mostly be determined by other series resistances, including those of the inter-flake interfaces and metal/semiconductor contacts,<sup>[9],[18]</sup> which are subject to change with the carrier concentration.

We tested various molecules to find an ideal p-type dopant to improve the performance of WSe<sub>2</sub> transistors. Originally, the WSe<sub>2</sub> films were washed with chloroform and bromoform solvent to remove any residual photoresist (PR), and we observed an improvement in transistor characteristics after the washing process (Figure S10). We then treated the devices with various halide-based molecules (Figure S10) and confirmed that Br<sub>2</sub> was the most effective p-type dopant for our WSe<sub>2</sub> films. For Br<sub>2</sub>-doped p-WSe<sub>2</sub> TFTs, the  $I_{DS}-V_{GS}$  transfer curve (Figure 2b) showed clear p-type characteristics, with a significantly improved hole  $\mu_{FE}$  of  $27 \text{ cm}^2 \text{ V}^{-1} \text{ s}^{-1}$  and a high on/off ratio of  $5 \times 10^7$ . The threshold voltage ( $V_{TH}$ ) showed a positive shift from  $-3.5 \text{ V}$  for the pristine to  $-0.1 \text{ V}$  for the doped p-WSe<sub>2</sub> TFTs, indicating a significant increase in the hole concentration after the Br<sub>2</sub> treatment. The electron transport was completely suppressed in the doped devices for all the TMDs used in this study. The output ( $I_{DS}-V_{DS}$ ) curve showed a linear response in the low  $V_{DS}$  region, indicating negligible contact resistance (Figure 2c). The Br<sub>2</sub> molecules effectively increased the hole concentration of the exfoliated 2D TMDs and led to efficient charge injection through tunneling from the Ni/Au to the highly doped channel. Additionally, we found that Br<sub>2</sub> doping is a more efficient method for solution-processed 2D p-WSe<sub>2</sub> TFTs than other treatment methods, such as interface treatment with UV-O<sub>3</sub> for WO<sub>x</sub> interlayers<sup>[7a]</sup> or defect engineering with HBr,<sup>[15a]</sup> TFSI,<sup>[19]</sup> and PEDOT:PSS,<sup>[20]</sup> The mobility ( $>10 \text{ cm}^2 \text{ V}^{-1} \text{ s}^{-1}$ ) and on-off ratio ( $>10^7$ ) of the

Br<sub>2</sub>-doped WSe<sub>2</sub> TFTs were much higher than the mobilities ( $\sim 0.1 \text{ cm}^2 \text{ V}^{-1} \text{ s}^{-1}$ ) and on-off ratios ( $\sim 10^5$ ) obtained by other treatment methods (Figure S11).

Accepted Article

According to the working mechanism of our solution-processed 2D TFTs, firstly, the charge carriers are injected from one metal contact to the 2D thin film semiconducting channel under the potential difference between source and drain terminals. Then, the electric current flows within the nanoflakes or across the narrow van der Waals gap between inter-flakes by hopping or tunneling to the other metal contact. The conductivity of the channel can be modulated by an external gate field. To understand the mechanism of mobility improvement using the Br<sub>2</sub> doping method, we first investigated the charge injection and contact resistance by temperature-dependent and four-point probe measurements. Generally, the direct deposition of metal electrodes by thermal evaporation on a WSe<sub>2</sub> layer results in a large Schottky barrier height of over 1 eV for hole injection owing to Fermi-level pinning.<sup>[21]</sup> However, our Br<sub>2</sub>-doped WSe<sub>2</sub> TFTs exhibited a very small Schottky barrier height of approximately 80 meV (Figure S12). This indicates that Br<sub>2</sub> doping enabled efficient hole injection from Ni into the 2D thin film. The total contact resistance ( $2R_c$ ) was measured using the four-point probe method (Figure 2d). The  $2R_c$  value significantly decreased from  $2.7 \times 10^5 \text{ k}\Omega \mu\text{m}$  in the pristine WSe<sub>2</sub> transistors to  $104 \text{ k}\Omega \mu\text{m}$  in the Br<sub>2</sub>-doped WSe<sub>2</sub> transistors at the  $10 \mu\text{M}$  doping concentration, and it showed much a smaller value of  $60 \text{ k}\Omega \mu\text{m}$  at a high doping concentration ( $25 \mu\text{M}$ ) (Figure S13). Such a small contact resistance in the heavily doped device is comparable to that of 2D devices with dry-transferred van der Waals metal contacts, as shown in Table S1.

We then analyzed the change in charge transport in the channel as a result of Br<sub>2</sub> doping by evaluating the trapped charge density, channel resistance ( $R_{\text{ch}}$ ), and activation energy ( $E_a$ ). The pristine WSe<sub>2</sub> TFTs exhibited a large hysteresis ( $\Delta V$ ) of 1.82 V in the transfer curve (Figure S14a), implying a high trapped charge density ( $3.4 \times 10^{12} \text{ cm}^{-2}$ ), which mainly originated from bubbles of trapped adsorbates at the gate insulator/semiconductor interface and interflake interfaces,<sup>[22]</sup> as confirmed by the AFM results (Figure S8b). With the Br<sub>2</sub> treatment, the hysteresis and trapped charge density decreased substantially to 0.49 V and 0.9



$\times 10^{12} \text{ cm}^2$ , respectively (Figure S14b), by filling the trap states near the valence band edge with doping carriers. Meanwhile, with excess carrier doping, the channel resistance of the  $\text{Br}_2$ -doped  $\text{WSe}_2$  TFTs decreased from  $6.2 \times 10^5 \text{ k}\Omega \mu\text{m}$  for the pristine  $\text{WSe}_2$  TFTs to 549 and 196  $\text{k}\Omega \mu\text{m}$  for the  $\text{WSe}_2$  TFTs with medium (10  $\mu\text{M}$ ) and high doping (25  $\mu\text{M}$ ) concentrations, respectively. (Figure 2d and Figure S13). Therefore, the doped TFTs showed reasonably low  $E_a$  values for hole transport of 32–85 meV for gate voltages from 0 V to -3 V (Figure 2e). This means that intra-flake charge transport was dominant rather than inter-flake hopping in the  $\text{Br}_2$ -doped TFTs,<sup>[23]</sup> indicating a low barrier for charge transport between the flakes. Thus, we concluded that there were two main reasons for the increased mobility in our solution-processed 2D TFTs: the first was the reduced contact resistance as a result of  $\text{Br}_2$  doping and the second was the improved charge transport in the channel as a result of the reduced channel resistance at the interfaces.  $\text{Br}_2$  molecules could be inserted into the inter-flake spaces owing to their smaller size<sup>[24]</sup> (Figure 2a). We thus determined that the molecular size of the dopant is crucial when selecting dopants for solution-processed 2D TFTs. Additionally, we anticipate that large lateral nanoflakes with a clean surface and a well-selected thickness distribution, and compact 2D nanoflake thin films would be helpful to reduce the total resistance for further improved solution-processed 2D TFTs in the near future, as they are associated with the conductivity of the single nanoflakes and the inter-flake junction.<sup>[3c]</sup>

To further investigate the molecular doping effects on the transport properties, we immersed the as-prepared 2D  $\text{WSe}_2$  film into diluted  $\text{Br}_2$  solutions at various concentrations (Figure 2f, Figure S15a). Changes in  $V_{\text{th}}$  indicated increased hole doping as the concentration of  $\text{Br}_2$  increased (Figure S15b). Along with the hole doping, the  $\mu_{\text{FE}}$  dramatically increased with the  $\text{Br}_2$  concentration at the low concentration level, reaching  $27 \text{ cm}^2 \text{ V}^{-1} \text{ s}^{-1}$  at 7.5  $\mu\text{M}$ , with a high on/off ratio of  $5 \times 10^7$ . It then slowly increased to  $40 \text{ cm}^2 \text{ V}^{-1} \text{ s}^{-1}$  at the higher concentration regime, with a decrease in the on/off ratio to  $\sim 10^3$ . The on/off ratio decreased at high doping concentrations because of the high off current induced by the increased carrier concentration. Under high doping conditions, this could create excess charges in the

semiconductor thin film, thereby increasing the conductivity of the channel. Consequently, a large positive bias must be applied to fully deplete the excess charges, which can compromise the on/off ratio of the transistor. On the other hand, the mobility enhancement produced by increasing the doping concentration was unexpected based on a band-transport scheme. We attributed this to the high resistance of a more significant number of inter-flake boundaries, which dominated the total charge transport across the entire WSe<sub>2</sub> semiconducting layer. The gate-induced conducting surfaces were vertically separated by the finite thicknesses of individual flakes, and the electrical connectivity was greatly influenced by the out-of-plane conductivity, including the inter-flake conductivity.

The Br<sub>2</sub>-doped WSe<sub>2</sub> TFTs showed similar mobilities for the two-point and four-point probe measurements, which were 28 and 34 cm<sup>2</sup> V<sup>-1</sup> s<sup>-1</sup>, respectively (Figure S13e). The slightly higher mobility for the four-point probe measurements is because  $2R_c$  was somewhat smaller than  $R_{CH}$ , and  $2R_c$  was much less dependent on  $V_{GS}$  compared with  $R_{CH}$ .<sup>[25]</sup> The Hall mobility for Br<sub>2</sub>-doped WSe<sub>2</sub> film which was measured using the Hall bar structure, was approximately 67 cm<sup>2</sup> V<sup>-1</sup> s<sup>-1</sup> (Figure 2d and Figure S16), which was slightly higher than the field-effect mobility. This is because the Hall mobility was obtained from the bulk transport mode, whereas the field-effect mobility was obtained from the interface transport mode.<sup>[26]</sup> The variance of the extracted mobility using different methods is discussed in detail in the Supporting Information. To evaluate the reliability of the devices and their reproducibility, we fabricated three batches of devices and measured 10 transistors from each batch for 30 transistors in total. The optimized doped p-WSe<sub>2</sub> TFTs exhibited excellent reproducibility, with an average  $\mu_{FE}$  of 27 cm<sup>2</sup> V<sup>-1</sup> s<sup>-1</sup> (highest: 33 cm<sup>2</sup> V<sup>-1</sup> s<sup>-1</sup>, two-point probe measurement), a high on/off ratio of over 10<sup>6</sup>, and an average near-zero  $V_{TH}$  (0.1 V) in 30 TFTs measurements (Figure 2f, Figure S17a-c). Meanwhile, the statistical histograms of the  $\mu_{FE}$  from different batches at different spatial locations (Figure S17d-e) show a small standard deviation indicating the high reproducibility of our doping method. In addition, we measured 7 TFTs to demonstrate the reliability of the  $\mu_{FE}$  extracted from two-probe and four-probe measurements (Figure S17f). The average mobility is 27.5 cm<sup>2</sup> V<sup>-1</sup> s<sup>-1</sup> for two-point probe

measurements and  $31.2 \text{ cm}^2 \text{ V}^{-1} \text{ s}^{-1}$  for four-point probe measurements. The performance of the p-WSe<sub>2</sub> TFTs achieved in this study is a record high to the best of our knowledge and is significantly larger than that of previously reported solution-processed p-WSe<sub>2</sub> TFTs (mobility of  $\sim 0.1 \text{ cm}^2 \text{ V}^{-1} \text{ s}^{-1}$  and on/off ratio of  $\sim 10^2$ ).<sup>[6a]</sup> Furthermore, it is comparable to the reported values for CVD-processed p-type 2H MoTe<sub>2</sub> TFTs (hole mobility of  $\sim 45 \text{ cm}^2 \text{ V}^{-1} \text{ s}^{-1}$  and on/off ratio of  $\sim 1.5 \times 10^4$ ).<sup>[27]</sup>

To verify the doping effect of Br<sub>2</sub> molecules on various p-type 2D TMDs, we measured the transport characteristics of WS<sub>2</sub>, MoSe<sub>2</sub>, and MoTe<sub>2</sub> TFTs before and after Br<sub>2</sub> chemical treatment (Figure S18). The pristine WS<sub>2</sub> and MoSe<sub>2</sub> TFTs exhibited typical n-type device characteristics, with corresponding electron mobilities of 1.8 and  $1.2 \text{ cm}^2 \text{ V}^{-1} \text{ s}^{-1}$ , respectively. After the Br<sub>2</sub> chemical treatment, typical p-type characteristics were observed in the WS<sub>2</sub> and MoSe<sub>2</sub> TFTs, with hole mobilities of 1 and  $4 \text{ cm}^2 \text{ V}^{-1} \text{ s}^{-1}$ , respectively. The same phenomenon was observed in MoTe<sub>2</sub> TFTs, with slightly lower hole mobility ( $0.1 \text{ cm}^2 \text{ V}^{-1} \text{ s}^{-1}$ ). These results suggested that Br<sub>2</sub> doping is generally applicable to various p-type TMDs, although the doping efficiencies could vary from material to material. We also observed that our Br<sub>2</sub> doping method worked with mechanically exfoliated single-flake-based WSe<sub>2</sub> transistors and CVD-grown monolayer transistors (Figure S19). The performances of the doped TFTs achieved in this study and those of previously reported solution-processed TMD-based TFTs are summarized in Figure S20 and Table S2 for comparison.

The stability of the Br<sub>2</sub>-doped WSe<sub>2</sub> TFTs was also investigated. First, we evaluated the on/off switching characteristics of the device (Figure 2g). The on and off states showed a constant current after 2000 s of consecutive on/off switching tests. Furthermore, after 100 cyclic sweeps, there was a negligible change in the transfer characteristics, with a max  $V_{\text{TH}}$  shift of only 0.07 V (Figure S21). We then characterized the bias-stress stability of the device at 20 °C and 60 °C (Figure S21). After biasing for 16,500 s at 20 °C with a constant applied gate voltage of -1 V, the  $V_{\text{TH}}$  of the device shifted by only -0.68 V. Even at a high temperature of 60 °C, the device showed a small  $V_{\text{TH}}$  shift of only -1.42 V. Therefore, we can conclude that the Br<sub>2</sub>-doped device showed excellent stability, indicating that the Br<sub>2</sub>

molecules were tightly attached to the WSe<sub>2</sub> thin film. In addition, we observed that the transfer characteristics of the Br<sub>2</sub>-doped transistors remained the same, even after the deposition of other polymer layers such as CYTOP and PMMA, which were used to evaluate the stability of follow-up processes, such as the back-end-of-line (BEOL) process (Figure S22).

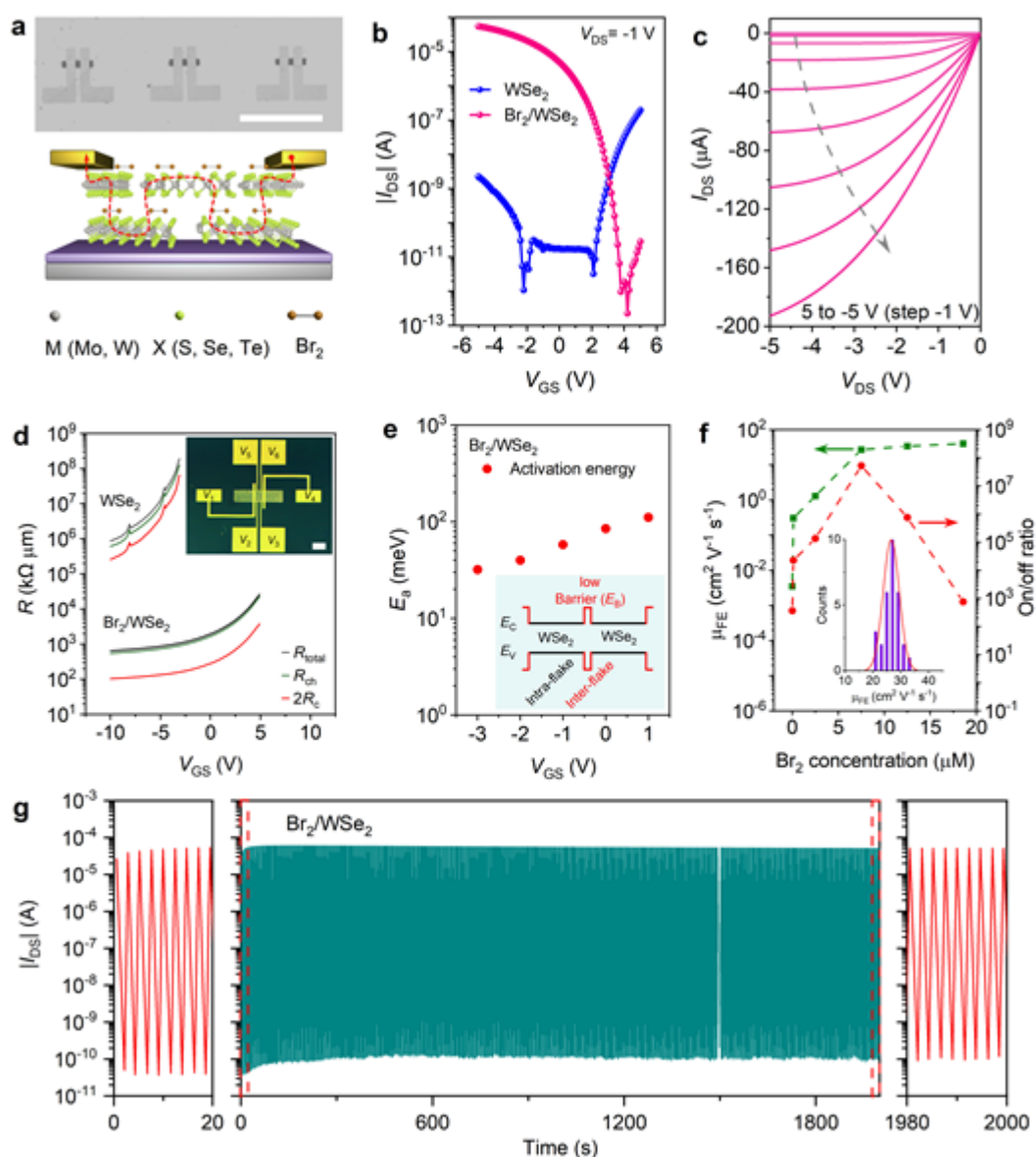


**Figure 2. Electrical characterizations of solution-processed WSe<sub>2</sub> transistors.** a, SEM image of the WSe<sub>2</sub> transistor array on the HfO<sub>2</sub>/Si substrate (scale bar, 1  $\mu\text{m}$ ). Schematic of cross-sectional transistor structure with Br<sub>2</sub> on the TMD surface and interface, where the red line indicates the charge transport pathway. b,  $I_{DS} - V_{GS}$  transfer curves at  $V_{DS} = -1$  V for the This article is protected by copyright. All rights reserved.

pristine and Br<sub>2</sub>-treated WSe<sub>2</sub> transistor. **c**, Output characteristic of the corresponding Br<sub>2</sub>-treated WSe<sub>2</sub> transistor. **d**, Extracted resistance from the four-probe measurement: total resistance ( $R_{\text{total}}$ ), channel resistance ( $R_{\text{ch}}$ ), and total contact resistance ( $2R_{\text{c}}$ ), for pristine device and medially Br<sub>2</sub> doped device (10  $\mu\text{M}$ ). Inset is a solution-processed WSe<sub>2</sub> TFT with a Hall bar structure (scale bar, 100  $\mu\text{m}$ ). Scale bar **e**, Activation energy  $E_{\text{a}}$  as a function of  $V_{\text{GS}}$ . Inset is the band diagram for the barrier between interflakes.  $E_{\text{c}}$ ,  $E_{\text{v}}$ , and  $E_{\text{B}}$  correspond to the conduction band edge energy, valence band edge energy, and barrier, respectively. **f**,  $\mu_{\text{FE}}$  and on/off ratio values for pristine and Br<sub>2</sub>-treated transistors with different Br<sub>2</sub> concentrations. Inset is the statistical histograms of  $\mu_{\text{FE}}$  for 30 transistors. **g**, On/off switching cycling test of one representative Br<sub>2</sub>/WSe<sub>2</sub> TFT.

To understand the Br<sub>2</sub> molecules doping principle for p-type 2D TMDs, photoelectron spectroscopy, and density functional theory (DFT) calculations were performed. **Figure 3a** and **b** (Figure S23) show the X-ray photoelectron spectroscopy (XPS) spectra of the W 4*f*, Se 3*d*, and Br 3*d* peaks before and after Br<sub>2</sub> treatment. The spectral shapes of the W and Se peaks were nearly identical after the Br<sub>2</sub> treatment, indicating that the treatment did not chemically change the WSe<sub>2</sub> flakes. This result was consistent with the change in the transfer curves after immersing the Br<sub>2</sub>-doped WSe<sub>2</sub> TFTs in acetone solvent (Figure S24). After immersing the WSe<sub>2</sub> TFTs in acetone for 30 min as a washing solvent for the Br<sub>2</sub>, the transfer characteristics of the WSe<sub>2</sub> TFTs almost returned to those of the original undoped devices because of the desorption of the Br<sub>2</sub> molecules from the WSe<sub>2</sub> surface. This result indicated that the Br<sub>2</sub> molecules were immobilized on the surfaces of the WSe<sub>2</sub> flakes by physisorption rather than chemisorption. The positions of the XPS main peaks for W 4*f* and Se 3*d* were downshifted with respect to the binding energy by  $\sim 0.30$  eV after the Br<sub>2</sub> treatment, indicating a shift in the Fermi level toward the valence band edge as a result of the p-type doping.<sup>[28]</sup> In addition, we performed XPS measurements on other 2D TMD materials, including WS<sub>2</sub>, MoSe<sub>2</sub>, and MoTe<sub>2</sub> (Figure 25). Interestingly, we observed only an obvious peak shift in the MoSe<sub>2</sub> film after the Br<sub>2</sub> treatment among the three TMD films.

This article is protected by copyright. All rights reserved.

We further investigated the electronic structure of the 2D TMDs after Br<sub>2</sub> doping using ultraviolet photoelectron spectroscopy (UPS) (Figure 3c). Based on the secondary electron cutoff spectrum, a downward shift of the Fermi level from -3.87 eV to -4.88 eV was observed after the Br<sub>2</sub> treatment of the WSe<sub>2</sub> film. The valence band maximum ( $E_{\text{VBM}}$ ) for the Fermi level ( $E_{\text{F}}$ ) also shifted from 1.45 to 0.47 eV. The energy-level diagrams for WSe<sub>2</sub> and Br<sub>2</sub>/WSe<sub>2</sub> are shown in Figure 3d. The downshift of  $E_{\text{F}}$  to  $E_{\text{VBM}}$  indicated significant electron transfer from the WSe<sub>2</sub> to Br<sub>2</sub> molecules, namely the p-type doping effect of the Br<sub>2</sub> molecules and was in good agreement with the above XPS results.

We also assessed the electronic structure changes in the other three 2D TMD materials (WS<sub>2</sub>, MoSe<sub>2</sub>, and MoTe<sub>2</sub>) by obtaining UPS results before and after the Br<sub>2</sub> treatment and produced corresponding energy-level diagrams for all four 2D TMD materials (Figure S26). All of the  $E_{\text{F}}$  values shifted toward the valence band after the Br<sub>2</sub> treatment, indicating a general p-doping effect of Br<sub>2</sub> molecules on these 2D TMD materials. For the MoTe<sub>2</sub> film, only a limited  $E_{\text{F}}$  shift was observed after the Br<sub>2</sub> treatment due to the oxidation of the exfoliated MoTe<sub>2</sub> flakes, as confirmed by the XPS results (Figure S25). Nevertheless, a more significant  $E_{\text{F}}$  shift was observed in the Br<sub>2</sub>-treated WSe<sub>2</sub> film after the same doping process compared to the other three Br<sub>2</sub>-treated 2D TMDs films, implying that more efficient doping occurred for the WSe<sub>2</sub>. Moreover, the electronic bands for the Br<sub>2</sub>/WSe<sub>2</sub> were best matched with the Ni/Au electrodes. Therefore, the XPS and UPS analyses explained why the best device performance was achieved in the Br<sub>2</sub>/WSe<sub>2</sub> TFTs compared to the other 2D TMDs.

To identify the possible Br<sub>2</sub> doping mechanism for the 2D TMDs used in this work, we performed DFT calculations. We considered various Br<sub>2</sub> adsorption configurations at various coverage values ( $\theta$ ). The Br<sub>2</sub> adsorption energy was calculated to be positive (preferably adsorbed) up to the saturation coverage,  $\theta_{\text{sat}}$  (Figure S27a). The most stable adsorption configuration close to  $\theta_{\text{sat}}$  is shown in Figure 3e; the Br<sub>2</sub> molecules lay in-plane on the WSe<sub>2</sub> surface. The calculated electronic structure of Br<sub>2</sub>/WSe<sub>2</sub> is compared with that of pristine WSe<sub>2</sub> in Figure 3f. Acceptor states were generated near the  $E_{\text{VBM}}$  in the bandgap. The shallow acceptor state was characterized by the Br<sub>2</sub>  $\sigma_{\text{p}}^*$  antibonding molecular orbital state, which

This article is protected by copyright. All rights reserved.

was empty. The calculated  $E_F$  shifted toward the  $E_{VBM}$  of  $WSe_2$  as a result of the  $Br_2$  adsorption, which was consistent with the  $E_F$  shift measured by UPS. As the  $Br_2$  coverage,  $\theta$ , increased, more acceptor states were available and more p-doping occurred, consistent with the electrical measurement results.

DFT calculations revealed the doping efficiencies of different diatomic halogen molecules, including  $I_2$ ,  $Br_2$ ,  $Cl_2$ , and  $F_2$ . The acceptor levels were found to be 0.05 ( $I_2$ ), 0.08 ( $Br_2$ ), 0.45 ( $Cl_2$ ), and 0.75 eV ( $F_2$ ) from the  $E_{VBM}$  of  $WSe_2$  (Figure S28a), indicating that both  $I_2$  and  $Br_2$  are good p-type dopants for  $WSe_2$ . We then dissolved the solid  $I_2$  powder into 1,2-dichlorobenzene and immersed the  $WSe_2$  TFTs into the solution. The  $I_2$ -doped  $WSe_2$  TFT exhibited an improved mobility of  $13 \text{ cm}^2 \text{ V}^{-1} \text{ s}^{-1}$  (Figure S28b). We also calculated the electronic structures of the  $Br_2$  molecules adsorbed on three other 2D TMDs:  $MoS_2$ ,  $WS_2$  and  $MoSe_2$  (Figure S27b). Acceptor-like in-gap states were created by the  $Br_2$  adsorption, but the empty  $Br_2 \sigma_p^*$  acceptor level deepened in the order  $WSe_2$ ,  $MoSe_2$ ,  $WS_2$ , and  $MoS_2$ , degrading the p-doping efficiency. The  $Br_2$  acceptor levels were found to be 0.08 ( $WSe_2$ ), 0.27 ( $MoSe_2$ ), 0.28 ( $WS_2$ ), and 0.51 eV ( $MoS_2$ ) from the  $E_{VBM}$  of each 2D TMD (Figure S27c). This result indicated that  $Br_2$  is an efficient p-type dopant for  $WSe_2$ , but  $MoS_2$  generates rather deep acceptor states. This result also explained the difference in the  $Br_2$  doping efficiencies for  $WS_2$ ,  $MoSe_2$ , and  $MoS_2$ .

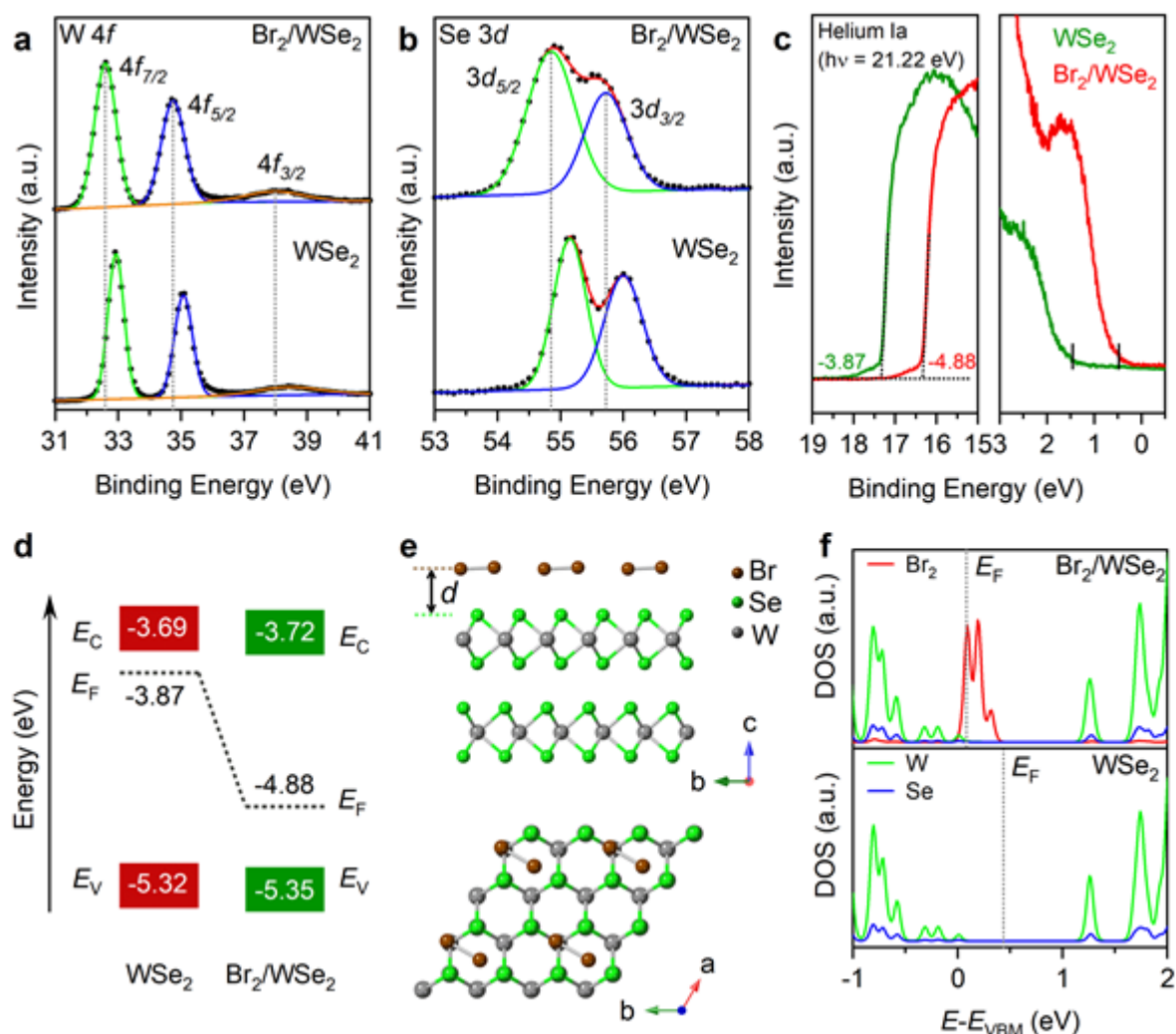


**Figure 3. Photoelectron spectroscopy and DFT calculation results.** **a, b**, XPS spectra of core-level W  $4f_{5/2}$  and  $4f_{7/2}$  binding energy peaks and Se  $3d_{3/2}$  and  $3d_{5/2}$  binding energy peaks before and after  $\text{Br}_2$  treatment. **c**, UPS spectra of secondary electron cutoff and valence band of pristine  $\text{WSe}_2$  and  $\text{Br}_2$ -treated  $\text{WSe}_2$  thin film. **d**, Corresponding schematic energy level diagrams. **e**, Adsorption configuration of  $\text{Br}_2$  on  $\text{WSe}_2$  optimized in DFT calculations, where the distance between the  $\text{Br}_2$  and nearest S atomic layer is  $d = 3.3 \text{ \AA}$ . **f**, Calculated electronic density of states of  $\text{Br}_2$ -adsorbed  $\text{WSe}_2$  (top) and pristine  $\text{WSe}_2$  (bottom). The Fermi level ( $E_F$ ) is shifted to  $E_{\text{VBM}}$  by the  $\text{Br}_2$ -induced shallow acceptor states (red curve). DOS for W atoms (green curve), Se atoms (blue curve), and  $\text{Br}_2$  (red curve).



We demonstrated a CMOS inverter composed of p-WSe<sub>2</sub> and n-MoS<sub>2</sub> TFTs (**Figure 4a**) with a lift-off-based patterning method. The n-MoS<sub>2</sub> films were formed from electrochemically exfoliated nanosheets using a large tetraheptylammonium bromide by the same drop-casting method as WSe<sub>2</sub>. Details of the fabrication process for the n-MoS<sub>2</sub> film and TFTs are described in the Methods section. The optimized n-MoS<sub>2</sub> TFTs exhibited an average mobility of 13 cm<sup>2</sup> V<sup>-1</sup> s<sup>-1</sup> with bis(trifluoromethane)sulfonimide (TFSI) treatment (Figure S29).<sup>[4, 29]</sup> To achieve a high inverter gain, the drain currents of the p-WSe<sub>2</sub> and n-MoS<sub>2</sub> TFTs were adjusted to the same level by controlling the channel width (Figure 4b). The CMOS inverters exhibited an ideal steep switching at the voltage transfer characteristics (VTC, Figure 4c). Extremely high voltage gains of 375, 790, and 1280 V were achieved under driving voltages ( $V_{DD}$ ) of 3, 5, and 7 V (Figure 4d). Thanks to the balanced electrical characteristics of p- and n-type TFTs, the switching thresholds ( $V_M$ ) at the  $V_{DD}$  of 3, 5, and 7 V were 1.86, 2.48, and 2.96, respectively, which were close to half of each  $V_{DD}$ . From the VTC result for  $V_{DD} = 5$  V (Figure 4e), we could further extract the noise margin low ( $NM_L$ ) of 2.17 V and noise margin high ( $NM_H$ ) of 2.26 V. The total noise margin can be expressed as  $(NM_L + NM_H)/V_{DD}$ ,<sup>[30]</sup> which is 88.6% for  $V_{DD} = 5$  V in the optimized inverter, indicating a high noise tolerance. Moreover, the CMOS inverter showed static currents lower than 0.1 nA at  $V_{IN} = 0$  V or  $V_{IN} = V_{DD}$ , which led to the low static power consumption of <1 nW (Figure S30). To the best of our knowledge, this is a record high gain value for mechanically exfoliated, CVD-processed, and solution-processed 2D material-based CMOS inverters, including TMDs, BP, Bi<sub>2</sub>O<sub>2</sub>Se, SnS<sub>2</sub>, InSe, and ReS<sub>2</sub> (Figure 4f, Figure S31, and Table S3). With further optimization of the subthreshold slope, such as reducing the defect trap density and increasing the gate insulator capacitance per unit area, we expect to achieve a higher gain and lower power consumption.<sup>[31]</sup>

The dynamic performance of the inverter was evaluated with a solution-processed five-stage ring oscillator (Figure 4g). Each n-type and p-type transistor has a channel length of 60  $\mu$ m and a HfO<sub>2</sub> gate dielectric thickness of 100 nm. Our five-stage ring oscillator exhibits a stable oscillation frequency ( $f$ ) of 1 kHz at a supply voltage of 25 V. The

corresponding stage delay ( $\tau = 1/(2Nf)$ ) is 100  $\mu\text{s}$ , where  $N$  is the number of inverter stages. The oscillation frequency of the ring oscillator can be improved by reducing the channel length of transistors and parasitic overlap capacitance between the gate-to-contact electrode.<sup>[32]</sup>

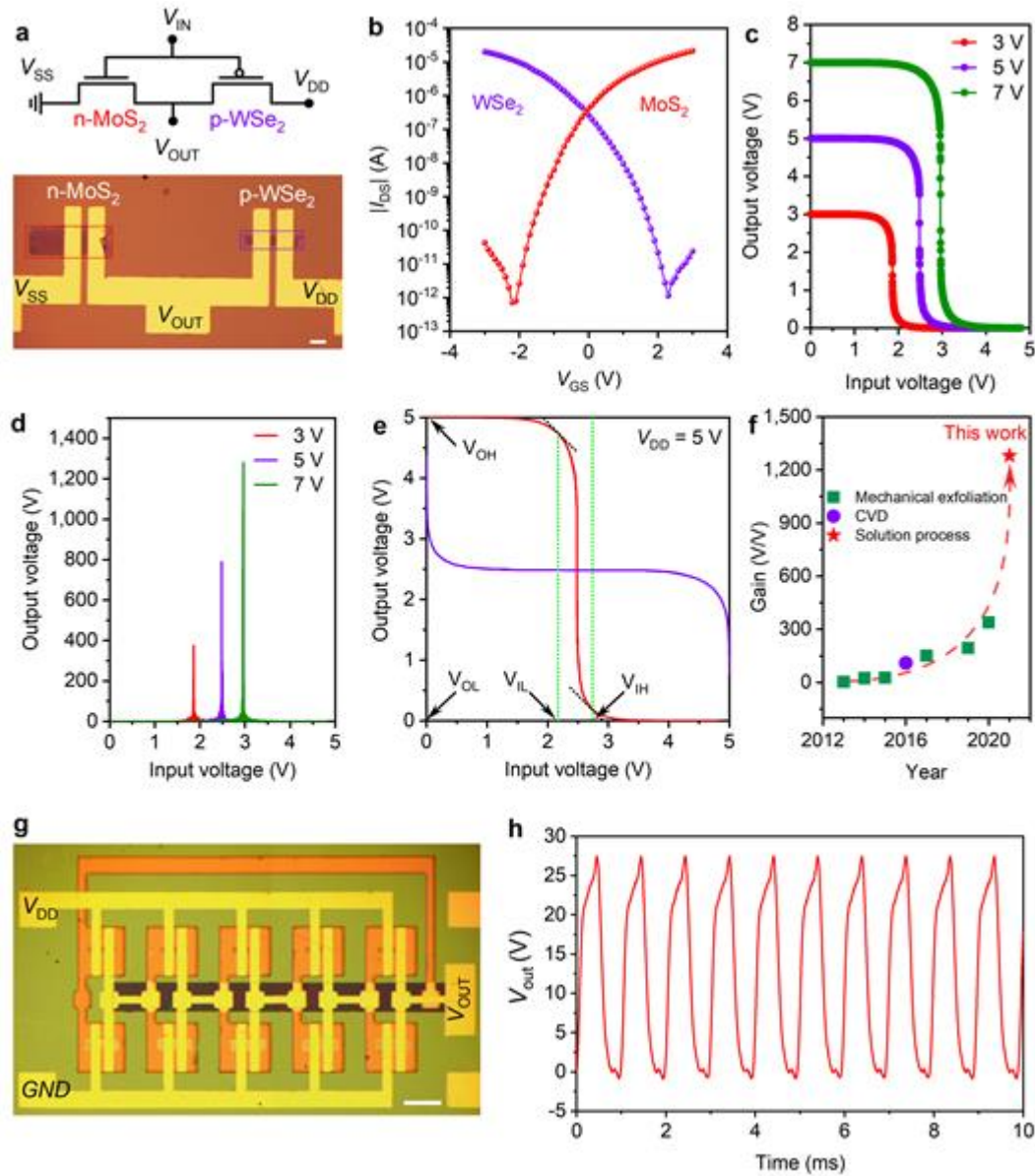


**Figure 4. Solution-processed CMOS Inverter and ring oscillator.** a, Circuit diagram of the complementary inverter (upper). False-colored optical microscope image of a solution-processed CMOS inverter (lower) (scale bar, 100  $\mu\text{m}$ ). b,  $I_{\text{DS}}-V_{\text{GS}}$  transfer curves of solution-processed p-WSe<sub>2</sub> and n-MoS<sub>2</sub> TFTs within the CMOS inverter. c, Voltage transfer characteristics of the CMOS inverter as a function of the input voltage with different  $V_{\text{DD}}$ . This article is protected by copyright. All rights reserved.

values of 3, 5, and 7 V. **d**, Corresponding gains of the inverter from **c**. **e**, Noise margin characteristics of the CMOS at  $V_{DD} = 5$  V. **f**, The reported highest gain for each year, where the gain was extracted from different 2D material-based CMOS inverters, such as TMDs, black phosphorene (BP),  $\text{SnS}_2$ , InSe,  $\text{ReS}_2$ , and  $\text{Bi}_2\text{O}_2\text{Se}$ , as listed in Table S2. **g**, False-colored optical microscope image of a solution-processed five-stage ring oscillator (scale bar, 500  $\mu\text{m}$ ). **h**, Output signal of a five-stage ring at  $V_{DD}$  values of 25 V.

### 3. conclusion

In conclusion, we have achieved high-performance p-type 2D  $\text{WSe}_2$  TFTs with high reliability and reproducibility by solution-based p-doping using halide molecules. By physically absorbing  $\text{Br}_2$  on the surface of 2D  $\text{WSe}_2$  through a simple solution-based doping process, it was possible to control the hole concentration over a wide range by the formation of acceptor states near the VBM of  $\text{WSe}_2$ . Because of its small molecular size,  $\text{Br}_2$  effectively doped the interfaces, which dramatically reduced the contact resistance through a low charge injection barrier and enabled efficient channel charge transport. The  $\text{Br}_2$ -doped  $\text{WSe}_2$  transistors show excellent operational stability, including on-off switching, cycling, and bias stressing. This scalable and versatile technique for fabricating high-performance p-type channels with excellent stability by solution processes can lead to the development of emerging devices on various platforms, including wearable biosensors and monolithic integrated circuitry on Si CMOS.

### 4. Experimental Section

**Ink Formulation.** The intercalation process was carried out in a two-electrode system with tetraethylammonium bromide cation as the electrolyte.<sup>[4]</sup> Specifically, a TMD crystal was attached to a copper plate with conductive copper tape as the cathode, while a graphite rod served as the anode. Tetraethylammonium bromide (THAB, 98% from TCI) was dissolved in

acetonitrile at a concentration of  $5 \text{ mg mL}^{-1}$  as the electrolyte. The voltage applied to the cathode was approximately  $-15 \text{ V}$  for 1 h during the intercalation process. Subsequently, the expanded TMD crystals were sonicated in 40 mL of a PVP/DMF solution at a concentration of  $8 \text{ mg mL}^{-1}$  for 30 min. We employed iterative centrifugation cascades to remove the intercalated molecules and large-size flakes.<sup>[17]</sup> The dispersion was centrifuged at 1000, 2000, and 3000 rpm for 30 min, and the precipitate was discarded. The sediment was collected at a centrifugation speed of 5000 rpm and dispersed in a certain amount of IPA solution.  $\text{WSe}_2$ ,  $\text{MoSe}_2$ ,  $\text{WS}_2$ , and  $\text{MoTe}_2$  crystals for electrochemical intercalation were purchased from 2D Semiconductors, USA, and  $\text{MoS}_2$  crystals from SPI Supplies were used as received.

**Thin-film deposition and device fabrication.** First, the SU8 photoresist was prepared on a 100 nm thick  $\text{SiO}_2/\text{Si}$  or 40 nm thick  $\text{HfO}_2/\text{Si}$  substrate using a conventional photolithography method to form the desired patterns. The  $\text{HfO}_2$  dielectric layer was deposited by atomic layer deposition (ALD) at a processing temperature of  $200 \text{ }^\circ\text{C}$ . TMD inks were drop-cast onto the patterned photoresist to confine the growth of the 2D thin film. The substrate was covered with a Petri dish to slow the solvent evaporation and obtain a well-stacked thin film. After the solvent was evaporated, the photoresist was removed with chloroform to obtain highly aligned 2D TMD thin-film arrays. Then, the substrate with the 2D thin-film arrays was annealed on a hotplate in a nitrogen-filled glovebox at  $200 \text{ }^\circ\text{C}$  for 1 h. Finally, Ni (20 nm)/Au (50 nm) electrodes were thermally evaporated and patterned via the photolithography method. All of the fabrication processes were completed under ambient conditions, except for the annealing step in the glovebox and electrode deposition in a high-vacuum chamber.

**$\text{Br}_2$ -treatment.** The as-prepared device was rinsed in a diluted  $\text{Br}_2$  solution in a 1,2-dichlorobenzene solvent at concentrations of 10–240  $\mu\text{M}$ . The device was immersed in a solution at  $150 \text{ }^\circ\text{C}$  for 30 min under ambient conditions. The concentration of the diluted  $\text{Br}_2$  solution should be optimized for different TMD materials to obtain the desired performance because the doping effect of the  $\text{Br}_2$  molecules varied from material to material. In our work, we found that a higher concentration was needed for  $\text{WS}_2$  and  $\text{MoSe}_2$  compared with  $\text{WSe}_2$  and  $\text{MoTe}_2$ .

**CMOS and ring oscillator fabrication.** The MoS<sub>2</sub> thin film was first deposited on a 60 nm thick HfO<sub>2</sub>/Si substrate, followed by the WSe<sub>2</sub> thin film, using the method described above. We found that the SU-8 photoresist could deteriorate the electrical properties of MoS<sub>2</sub>, but do not influence WSe<sub>2</sub>. Subsequently, the MoS<sub>2</sub> and WSe<sub>2</sub> thin films were treated together with 10 mg mL<sup>-1</sup> bis(trifluoromethane)sulfonimide (TFSI, Sigma-Aldrich) dissolved in 1,2-dichloroethane at 80 °C for 20 min.<sup>[4]</sup> The treated thin film was baked at 200 °C for 1 h. Finally, Ni (20 nm)/Au (50 nm) electrodes were thermally evaporated and patterned via photolithography. In the CMOS, the MoS<sub>2</sub> transistor showed an n-type behavior; however, the WSe<sub>2</sub> transistor still exhibited an n-type dominated feature. To achieve a balanced electrical property, we further converted the WSe<sub>2</sub> transistor into a p-type transistor by Br<sub>2</sub> solution treatment, with the MoS<sub>2</sub> covered with photoresist. For the ring oscillator, patterned Ni (5 nm)/Au (35 nm) electrodes were thermally evaporated on SiO<sub>2</sub> (300 nm)/Si substrate, then 100 nm HfO<sub>2</sub> was deposited by ALD. The WSe<sub>2</sub> and MoS<sub>2</sub> thin film active layer are fabricated, respectively. Finally, Ni (20 nm)/Au (100 nm) electrodes were thermally evaporated and patterned via photolithography.

**Characterizations.** The morphology and thickness were characterized using HR-SEM (JSM 7401F) and AFM (Digital Instruments Multimode IIIa). UV–vis absorption spectra were measured using a UV/vis/NIR spectroscope (JASCO V-770). Raman spectra were recorded using a Raman spectrometer (WiTec, with 532 nm laser excitation). XRD measurements were obtained using a Rigaku Ultima V diffractometer for a drop-cast thin film on a Si/SiO<sub>2</sub> substrate. XPS and UPS were performed at the Korea Basic Science Institute in Jeonju, Korea. XPS spectra were obtained using a monochromatic Al K $\alpha$  X-ray source ( $h\nu = 1486.7$  eV). UPS measurements were conducted using a He I (21.2 eV) source. Diluted TMD solutions were drop-cast onto a carbon-coated Cu TEM grid for TEM observations using a JEOL JEM 2100F. A cross-sectional TEM sample was prepared using a focused ion beam (Helios Nanolab 650, FEI) with Ni (20 nm)/Au (50 nm) on the surface of a 2D thin film for protection. The electrical characteristics of the transistors were measured using a Keithley 4200 parameter analyzer in an N<sub>2</sub>-filled glovebox (at 25 °C, O<sub>2</sub> and H<sub>2</sub>O levels: 5–10 ppm).

The bias stress measurement at 60 °C and the temperature-dependent measurement were measured under a vacuum condition ( $\sim 5 \times 10^{-3}$  Torr). All devices were measured without encapsulations. The transconductance ( $g_m$ ), field-effect mobility ( $\mu_{FE}$ ), and hole concentration ( $n_h$ ) were extracted, using the following:<sup>[33]</sup>

$$g_m = dI_{DS}/dV_{GS}, \quad (1)$$

$$\mu_{FE} = -g_m L / (V_{DS} C_{ox} W), \quad (2)$$

$$n_h = (I_{DS} L) / (q W V_{DS} \mu), \quad (3)$$

where  $L$  is the channel length,  $W$  is the channel width, and  $q$  is the electron charge. The hole concentration ( $n_h$ ) was calculated at  $V_{GS} = 0$  V and  $V_{GS} = -5$  V.  $C_{ox}$  is the gate dielectric capacitance per unit area and was measured experimentally using the standard capacitance–voltage (C-V) mode, which showed values of  $\sim 3 \times 10^{-7}$  F cm<sup>-2</sup> for 40 nm HfO<sub>2</sub> and  $3.4 \times 10^{-8}$  F cm<sup>-2</sup> for 100 nm SiO<sub>2</sub>. To evaluate the reliability and reproducibility, we fabricated three batches of devices and we measured 10 transistors from each batch for 30 transistors in total.

The mobility, total resistance ( $R_{total}$ ), channel resistance ( $R_{ch}$ ), and total contact resistance ( $2R_c$ ) were calculated from four-probe measurements with the following expressions:<sup>[34]</sup>

$$R_{total} = R_{ch} + 2R_c \quad (4)$$

$$R_{total} = (V_{14}/I_{DS})W, \quad (5)$$

$$R_{ch} = (V_{23}/I_{DS}) (L_{14}/L_{23})W, \quad (6)$$

$$\mu_{FE,4p} = -g_m L_{23} / (V_{23} C_{ox} W), \quad (7)$$

Where,  $L_{14}$  and  $V_{14}$  are the distance and voltage difference, respectively, between contacts 1 and 4 in the device.  $L_{23}$  and  $V_{23}$  are the distance and voltage difference, respectively, between contacts 2 and 3 in the middle of the device. We measured 7 devices to demonstrate the reliability of the  $\mu_{\text{FE}}$  extracted from two-probe and four-probe measurements.

The Schottky barrier  $\Phi_{\text{SB}}$  and activation energy ( $E_a$ ) can be extracted with the following equation:<sup>[35]</sup>

$$\ln\left(\frac{I_{\text{DS}}}{T^2}\right) = -\frac{\Phi_{\text{SB}}}{kT} + c \quad (8)$$

$$G(T) = G_0 e^{-E_a/kT} \quad (9)$$

where  $G$  is conductance,  $k$  is the Boltzmann constant.

**DFT calculations.** Density functional theory calculations were performed as implemented in the Vienna ab initio simulation package (VASP) code.<sup>[36]</sup> The projector-augmented wave (PAW) pseudopotentials<sup>[37]</sup> and a kinetic energy cutoff of 500 eV were applied. The Perdew, Burke, and Ernzerhof (PBE) functional within the generalized gradient approximation (GGA) was used for the exchange-correlation functional,<sup>[38]</sup> and the vdW-D2 correction proposed by Grimme was used to describe the long-range van der Waals interaction.<sup>[39]</sup> The bilayer TMDs were used with a vacuum thickness of 15 Å. To describe the various adsorption coverages of Br<sub>2</sub> molecules, 1 × 1, 2 × 2, 3 × 3, 4 × 4, and 6 × 6 supercells were considered. A  $\Gamma$ -centered 6 × 6 × 1 k-point mesh in the 1 × 1 supercell and its equivalent in the 2 × 2, 3 × 3, and 6 × 6 supercells were used for the Brillouin zone (BZ) summation. The  $\Gamma$  k-point was used in the 4 × 4 supercell. The Hellmann–Feynman forces were relaxed to less than 0.001 eV/Å. The optimized hexagonal lattice constants of WSe<sub>2</sub>, MoSe<sub>2</sub>, WS<sub>2</sub>, and MoS<sub>2</sub> were 3.328, 3.315, 3.180, and 3.188 Å, respectively. The calculation was performed with the DFT exchange-correlation functional of PBE-d2, which is known to underestimate the bandgap compared to the experimental bandgap. Since we are dealing with VBM and equilibrium

conditions (not dealing with excited conditions), disagreement in CBM placement will not be critical to presenting our point.

### Supporting Information

Supporting Information is available from the Wiley Online Library or from the author.

### Acknowledgements

This study was supported by the Ministry of Science and ICT through the National Research Foundation, funded by the Korean government (2020M3D1A1110548 and 2020M3D1A1110549). T. Y. Z gratefully acknowledges Dr. Mingchong Dai and Dr. Songbin Cui (POSTECH) for their helpful discussions.

### Conflict of Interest

The authors declare no competing financial interest.

Received: ((will be filled in by the editorial staff))

Revised: ((will be filled in by the editorial staff))

Published online: ((will be filled in by the editorial staff))

### References

- [1] a) C. Liu, H. Chen, S. Wang, Q. Liu, Y. G. Jiang, D. W. Zhang, M. Liu, P. Zhou, *Nat. Nanotechnol.* **2020**, *15*, 545; b) D. Akinwande, C. Huyghebaert, C. H. Wang, M. I. Serna, S. Goossens, L. J. Li, H. P. Wong, F. H. L. Koppens, *Nature* **2019**, *573*, 507; c) Y. Liu, X.



Duan, H.-J. Shin, S. Park, Y. Huang, X. Duan, *Nature* **2021**, *591*, 43; d) Y. Liu, Y. Huang, X. Duan, *Nature* **2019**, *567*, 323.

[2] a) S. Yang, P. Zhang, A. S. Nia, X. Feng, *Adv. Mater.* **2020**, *32*, e1907857; b) J. H. Han, M. Kwak, Y. Kim, J. Cheon, *Chem. Rev.* **2018**, *118*, 6151; c) J. Zheng, H. Zhang, S. Dong, Y. Liu, C. Tai Nai, H. Suk Shin, H. Young Jeong, B. Liu, K. Ping Loh, *Nat. Commun.* **2014**, *5*, 2995; d) J. Li, P. Song, J. Zhao, K. Vaklinova, X. Zhao, Z. Li, Z. Qiu, Z. Wang, L. Lin, M. Zhao, T. S. Heng, Y. Zuo, W. Jonhson, W. Yu, X. Hai, P. Lyu, H. Xu, H. Yang, C. Chen, S. J. Pennycook, J. Ding, J. Teng, A. H. Castro Neto, K. S. Novoselov, J. Lu, *Nat. Mater.* **2021**, *20*, 181; e) V. Nicolosi, M. Chhowalla, M. G. Kanatzidis, M. S. Strano, J. N. Coleman, *Science* **2013**, *340*, 1420.

[3] a) Z. Lin, Y. Huang, X. Duan, *Nat. Electron.* **2019**, *2*, 378; b) G. Hu, J. Kang, L. W. T. Ng, X. Zhu, R. C. T. Howe, C. G. Jones, M. C. Hersam, T. Hasan, *Chem. Soc. Rev.* **2018**, *47*, 3265; c) A. C. Kelly, D. O'Suilleabhain, C. Gabbett, J. N. Coleman, *Nat. Rev. Mater.* **2022**, *7*, 217; d) S. Pinilla, J. Coelho, K. Li, J. Liu, V. Nicolosi, *Nat. Rev. Mater.* **2022**, *7*, 717.

[4] Z. Lin, Y. Liu, U. Halim, M. Ding, Y. Liu, Y. Wang, C. Jia, P. Chen, X. Duan, C. Wang, F. Song, M. Li, C. Wan, Y. Huang, X. Duan, *Nature* **2018**, *562*, 254.

[5] A. Ziletti, A. Carvalho, D. K. Campbell, D. F. Coker, A. H. Castro Neto, *Phys. Rev. Lett.* **2015**, *114*, 046801.

[6] a) A. G. Kelly, T. Hallam, C. Backes, A. Harvey, A. S. Esmaily, I. Godwin, J. Coelho, V. Nicolosi, J. Lauth, A. Kulkarni, S. Kinge, L. D. Siebbeles, G. S. Duesberg, J. N. Coleman, *Science* **2017**, *356*, 69; b) G. Liu, C. Jin, B. Hu, L. Zhang, G. Zeng, H. Xu, *J. Mater. Chem. C* **2022**, *10*, 1526.

[7] a) M. Yamamoto, S. Nakaharai, K. Ueno, K. Tsukagoshi, *Nano Lett.* **2016**, *16*, 2720; b) A. N. Hoffman, M. G. Stanford, M. G. Sales, C. Zhang, I. N. Ivanov, S. J. McDonnell, D. G. Mandrus, P. D. Rack, *2D Materials* **2019**, *6*, 045024.

- [8] D. C. Moore, A. Jawaid, R. Busch, M. Brothers, P. Miesle, A. Miesle, R. Rao, J. Lee, L. K. Beagle, M. Motala, S. G. Wallace, J. R. Downing, A. Roy, C. Muratore, M. C. Hersam, R. Vaia, S. Kim, N. R. Glavin, *Adv. Funct. Mater.* **2022**, *32*, 2106830.
- [9] S. Ippolito, A. G. Kelly, R. Furlan de Oliveira, M.-A. Stoeckel, D. Iglesias, A. Roy, C. Downing, Z. Bian, L. Lombardi, Y. A. Samad, V. Nicolosi, A. C. Ferrari, J. N. Coleman, P. Samorì, *Nat. Nanotechnol.* **2021**, *16*, 592.
- [10] a) Y. Xu, C. Cheng, S. Du, J. Yang, B. Yu, J. Luo, W. Yin, E. Li, S. Dong, P. Ye, X. Duan, *ACS Nano* **2016**, *10*, 4895; b) A. Allain, J. Kang, K. Banerjee, A. Kis, *Nat. Mater.* **2015**, *14*, 1195; c) Q. He, Y. Liu, C. Tan, W. Zhai, G. H. Nam, H. Zhang, *ACS Nano* **2019**, *13*, 12294.
- [11] J. Suh, T. E. Park, D. Y. Lin, D. Fu, J. Park, H. J. Jung, Y. Chen, C. Ko, C. Jang, Y. Sun, R. Sinclair, J. Chang, S. Tongay, J. Wu, *Nano Lett.* **2014**, *14*, 6976.
- [12] a) S. Bertolazzi, M. Gobbi, Y. Zhao, C. Backes, P. Samori, *Chem. Soc. Rev.* **2018**, *47*, 6845; b) M.-Y. Tsai, S. Zhang, P. M. Campbell, R. R. Dasari, X. Ba, A. Tarasov, S. Graham, S. Barlow, S. R. Marder, E. M. Vogel, *Chem. Mater.* **2017**, *29*, 7296.
- [13] J. S. Ross, P. Klement, A. M. Jones, N. J. Ghimire, J. Yan, D. G. Mandrus, T. Taniguchi, K. Watanabe, K. Kitamura, W. Yao, D. H. Cobden, X. Xu, *Nat. Nanotechnol.* **2014**, *9*, 268.
- [14] a) D. H. Kang, J. Shim, S. K. Jang, J. Jeon, M. H. Jeon, G. Y. Yeom, W. S. Jung, Y. H. Jang, S. Lee, J. H. Park, *ACS Nano* **2015**, *9*, 1099; b) J. K. Kim, K. Cho, J. Jang, K. Y. Baek, J. Kim, J. Seo, M. Song, J. Shin, J. Kim, S. S. P. Parkin, J. H. Lee, K. Kang, T. Lee, *Adv. Mater.* **2021**, *33*, e2101598.
- [15] a) H. V. Han, A. Y. Lu, L. S. Lu, J. K. Huang, H. Li, C. L. Hsu, Y. C. Lin, M. H. Chiu, K. Suenaga, C. W. Chu, H. C. Kuo, W. H. Chang, L. J. Li, Y. Shi, *ACS Nano* **2016**, *10*, 1454; b) P. Zhao, D. Kiriya, A. Azcatl, C. Zhang, M. Tosun, Y.-S. Liu, M. Hettick, J. S. Kang, S. McDonnell, S. Kc, J. Guo, K. Cho, R. M. Wallace, A. Javey, *ACS Nano* **2014**, *8*, 10808.

- [16] M. Yamamoto, S. Dutta, S. Aikawa, S. Nakaharai, K. Wakabayashi, M. S. Fuhrer, K. Ueno, K. Tsukagoshi, *Nano Lett.* **2015**, *15*, 2067.
- [17] C. Backes, B. M. Szydłowska, A. Harvey, S. Yuan, V. Vega-Mayoral, B. R. Davies, P. L. Zhao, D. Hanlon, E. J. Santos, M. I. Katsnelson, W. J. Blau, C. Gadermaier, J. N. Coleman, *ACS Nano* **2016**, *10*, 1589.
- [18] K. Cho, J. Pak, S. Chung, T. Lee, *ACS Nano* **2019**, *13*, 9713.
- [19] H. Lu, A. Kummel, J. Robertson, *APL Mater.* **2018**, *6*, 066104.
- [20] X. Zhang, Q. Liao, S. Liu, Z. Kang, Z. Zhang, J. Du, F. Li, S. Zhang, J. Xiao, B. Liu, Y. Ou, X. Liu, L. Gu, Y. Zhang, *Nat. Commun.* **2017**, *8*, 15881.
- [21] G. Kwon, Y.-H. Choi, H. Lee, H.-S. Kim, J. Jeong, K. Jeong, M. Baik, H. Kwon, J. Ahn, E. Lee, M.-H. Cho, *Nat. Electron.* **2022**, *5*, 241.
- [22] a) Q. A. Vu, S. Fan, S. H. Lee, M.-K. Joo, W. J. Yu, Y. H. Lee, *2D Materials* **2018**, *5*, 031001; b) S. J. Haigh, A. Gholinia, R. Jalil, S. Romani, L. Britnell, D. C. Elias, K. S. Novoselov, L. A. Ponomarenko, A. K. Geim, R. Gorbachev, *Nat. Mater.* **2012**, *11*, 764; c) F. Pizzocchero, L. Gammelgaard, B. S. Jessen, J. M. Caridad, L. Wang, J. Hone, P. Bøggild, T. J. Booth, *Nat. Commun.* **2016**, *7*, 11894.
- [23] E. Piatti, A. Arbab, F. Galanti, T. Carey, L. Anzi, D. Spurling, A. Roy, A. Zhussupbekova, K. A. Patel, J. M. Kim, D. Daghero, R. Sordan, V. Nicolosi, R. S. Gonnelli, F. Torrisi, *Nat. Electron.* **2021**, *4*, 893.
- [24] a) Z. Chen, P. Darancet, L. Wang, A. C. Crowther, Y. Gao, C. R. Dean, T. Taniguchi, K. Watanabe, J. Hone, C. A. Marianetti, L. E. Brus, *ACS Nano* **2014**, *8*, 2943; b) N. Jung, N. Kim, S. Jockusch, N. J. Turro, P. Kim, L. Brus, *Nano Lett.* **2009**, *9*, 4133.
- [25] C. Liu, G. Li, R. Di Pietro, J. Huang, Y.-Y. Noh, X. Liu, T. Minari, *Phys. Rev. Appl.* **2017**, *8*, 034020.

- [26] A. Liu, H. Zhu, S. Bai, Y. Reo, T. Zou, M.-G. Kim, Y.-Y. Noh, *Nat. Electron.* **2022**, *5*, 78.
- [27] X. Xu, Y. Pan, S. Liu, B. Han, P. Gu, S. Li, W. Xu, Y. Peng, Z. Han, J. Chen, P. Gao, Y. Ye, *Science* **2021**, *372*, 195.
- [28] a) H. G. Ji, P. Solis-Fernandez, D. Yoshimura, M. Maruyama, T. Endo, Y. Miyata, S. Okada, H. Ago, *Adv. Mater.* **2019**, *31*, e1903613; b) S. Zhang, H. M. Hill, K. Moudgil, C. A. Richter, A. R. Hight Walker, S. Barlow, S. R. Marder, C. A. Hacker, S. J. Pookpanratana, *Adv. Mater.* **2018**, *30*, e1806345.
- [29] M. Amani, D. H. Lien, D. Kiriya, J. Xiao, A. Azcatl, J. Noh, S. R. Madhupathy, R. Addou, S. Kc, M. Dubey, K. Cho, R. M. Wallace, S. C. Lee, J. H. He, J. W. Ager, 3rd, X. Zhang, E. Yablonovitch, A. Javey, *Science* **2015**, *350*, 1065.
- [30] a) L. Kong, X. Zhang, Q. Tao, M. Zhang, W. Dang, Z. Li, L. Feng, L. Liao, X. Duan, Y. Liu, *Nat. Commun.* **2020**, *11*, 1866; b) H. J. Yun, J. Lim, J. Roh, D. C. J. Neo, M. Law, V. I. Klimov, *Nat. Commun.* **2020**, *11*, 5280.
- [31] a) Z. Luo, B. Peng, J. Zeng, Z. Yu, Y. Zhao, J. Xie, R. Lan, Z. Ma, L. Pan, K. Cao, Y. Lu, D. He, H. Ning, W. Meng, Y. Yang, X. Chen, W. Li, J. Wang, D. Pan, X. Tu, W. Huo, X. Huang, D. Shi, L. Li, M. Liu, Y. Shi, X. Feng, P. K. L. Chan, X. Wang, *Nat. Commun.* **2021**, *12*, 1928; b) C. Jiang, H. W. Choi, X. Cheng, H. Ma, D. Hasko, A. Nathan, *Science* **2019**, *363*, 719.
- [32] a) J. W. Borchert, B. Peng, F. Letzkus, J. N. Burghartz, P. K. L. Chan, K. Zojer, S. Ludwigs, H. Klauk, *Nat. Commun.* **2019**, *10*, 1119; b) J. W. Borchert, U. Zschieschang, F. Letzkus, M. Giorgio, R. T. Weitz, M. Caironi, J. N. Burghartz, S. Ludwigs, H. Klauk, *Sci Adv* **2020**, *6*, eaaz5156.
- [33] a) D. Lee, J. J. Lee, Y. S. Kim, Y. H. Kim, J. C. Kim, W. Huh, J. Lee, S. Park, H. Y. Jeong, Y. D. Kim, C.-H. Lee, *Nat. Electron.* **2021**, *4*, 664; b) E. Wu, Y. Xie, J. Zhang, H. Zhang, X. Hu, J. Liu, C. Zhou, D. Zhang, *Sci. Adv.* **2019**, *5*, eaav3430.

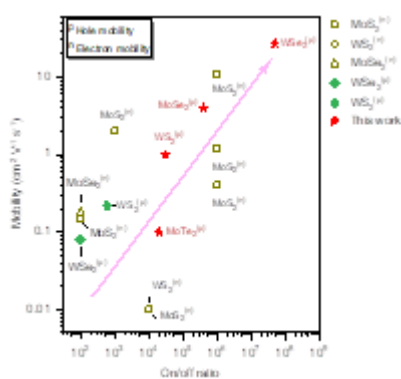
This article is protected by copyright. All rights reserved.

- [34] Y. Jung, M. S. Choi, A. Nipane, A. Borah, B. Kim, A. Zangiabadi, T. Taniguchi, K. Watanabe, W. J. Yoo, J. Hone, J. T. Teherani, *Nat. Electron.* **2019**, *2*, 187.
- [35] a) Y. Liu, J. Guo, E. Zhu, L. Liao, S. J. Lee, M. Ding, I. Shakir, V. Gambin, Y. Huang, X. Duan, *Nature* **2018**, *557*, 696; b) B. Radisavljevic, A. Kis, *Nat. Mater.* **2013**, *12*, 815.
- [36] G. Kresse, J. Furthmüller, *Phys. Rev. B* **1996**, *54*, 11169.
- [37] a) P. E. Blöchl, *Phys. Rev. B* **1994**, *50*, 17953; b) G. Kresse, D. Joubert, *Phys. Rev. B* **1999**, *59*, 1758.
- [38] J. P. Perdew, K. Burke, M. Ernzerhof, *Phys. Rev. Lett.* **1996**, *77*, 3865.
- [39] a) S. Grimme, J. Antony, S. Ehrlich, H. Krieg, *The Journal of Chemical Physics* **2010**, *132*, 154104; b) S. Grimme, S. Ehrlich, L. Goerigk, *J. Comput. Chem.* **2011**, *32*, 1456.

Solution-processed high-performance p-type WSe<sub>2</sub> thin-film transistor is successfully fabricated by Br<sub>2</sub>-doping with a field-effect hole mobility of more than 27 cm<sup>2</sup> V<sup>-1</sup> s<sup>-1</sup>, and a high on/off current ratio of ~10<sup>7</sup>. The resulting complementary inverters with patterned p-type WSe<sub>2</sub> and n-type MoS<sub>2</sub> layered films reaches an ultra-high gain of 1280 under a driving voltage (V<sub>DD</sub>) of 7 V.

Taoyu Zou<sup>1</sup>, Hyun-Jun Kim<sup>1</sup>, Soonhyo Kim<sup>1,2</sup>, Ao Liu<sup>1</sup>, Min-Yeong Choi<sup>1</sup>, Haksoon Jung<sup>1</sup>, Huihui Zhu<sup>1</sup>, Insang You<sup>1</sup>, Youjin Reo<sup>1</sup>, Woo-Ju Lee<sup>1</sup>, Yong-Sung Kim<sup>2,3\*</sup>, Cheol-Joo Kim<sup>1\*</sup>, Yong-Young Noh<sup>1\*</sup>

### High-performance solution-processed 2D p-type WSe<sub>2</sub> transistors and circuits through molecular doping



ToC figure